



AMERICAN METEOROLOGICAL SOCIETY

Journal of Physical Oceanography

EARLY ONLINE RELEASE

This is a preliminary PDF of the author-produced manuscript that has been peer-reviewed and accepted for publication. Since it is being posted so soon after acceptance, it has not yet been copyedited, formatted, or processed by AMS Publications. This preliminary version of the manuscript may be downloaded, distributed, and cited, but please be aware that there will be visual differences and possibly some content differences between this version and the final published version.

The DOI for this manuscript is doi: 10.1175/JPO-D-17-0194.1

The final published version of this manuscript will replace the preliminary version at the above DOI once it is available.

If you would like to cite this EOR in a separate work, please use the following full citation:

Ezhova, E., C. Cenedese, and L. Brandt, 2018: Dynamics of three-dimensional turbulent wall plumes and implications for estimates of submarine glacier melting. *J. Phys. Oceanogr.* doi:10.1175/JPO-D-17-0194.1, in press.

© 2018 American Meteorological Society



1 **Dynamics of three-dimensional turbulent wall plumes**
2 **and implications for estimates of submarine glacier melting**

3 Ekaterina Ezhova*

4 *Institute for Atmospheric and Earth System Research/Physics,*
5 *Faculty of Science, University of Helsinki, Finland.*

6 Claudia Cenedese

7 *Physical Oceanography Department, Woods Hole Oceanographic Institution,*
8 *Woods Hole, Massachusetts, USA*

9 Luca Brandt

10 *Linné FLOW Centre and SeRC (Swedish e-Science Research Centre),*
11 *KTH Mechanics, Stockholm, Sweden*

12 *Corresponding author address: Ekaterina Ezhova

13 E-mail: ekaterina.ezhova@helsinki.fi

ABSTRACT

14 Subglacial discharges have been observed to generate buoyant plumes along
15 the ice face of Greenland tidewater glaciers. These plumes have been tra-
16 ditionally modelled using classical plume theory and their characteristics
17 parameters, i.e. velocity, are employed in the widely used three-equation
18 melt parametrization. However, the applicability of plume theory for three-
19 dimensional turbulent wall plumes is questionable due to the complex near-
20 wall plume dynamics. In this study, corrections to the classical plume theory
21 are introduced to account for the presence of a wall. In particular, the drag and
22 entrainment coefficients are quantified for a three-dimensional turbulent wall
23 plume using data from direct numerical simulations. The drag coefficient is
24 found to be an order of magnitude larger than that for a boundary layer flow
25 over a flat plate at a similar Reynolds number. This suggests a significant in-
26 crease in the melting estimates by the current parametrization. However, the
27 volume flux in a wall plume is found to be half that of a conical plume which
28 has double the buoyancy flux. This suggests that the total entrainment (per
29 unit area) of ambient water is the same and that the plume scalar character-
30 istics, i.e. temperature and salinity, can be predicted reasonably well using
31 classical plume theory.

32 1. Introduction

33 Subglacial discharge is among the major factors controlling submarine melting of Greenland's
34 tidewater glaciers (Straneo and Cenedese 2015). Turbulent plumes generated by fresh water at the
35 freezing temperature discharged at the glacier base enhance melting of the ice face. In Greenland
36 the ice tongue has broken off in most tidewater glaciers and the ice face is quasi vertical, thus,
37 subglacial discharge plumes are usually modelled as a turbulent buoyant plume propagating along
38 a vertical ice face (Straneo and Cenedese 2015).

39 Current ice-ocean models quantify melting employing the three-equation formulation by Hol-
40 land and Jenkins (1999), where the effect of plume turbulence is parametrized through the friction
41 velocity u_* , a fundamental parameter defining wall-bounded turbulence, and the melting rate is
42 assumed to be proportional to u_* . To estimate the friction velocity from the mean velocity profile
43 a drag coefficient is typically used

$$C_d = \frac{\tau}{\rho U_{ref}^2} = \frac{u_*^2}{U_{ref}^2}, \quad (1)$$

44 where $\tau = \rho \langle u'_i u'_j \rangle$ is the mean turbulent stress parallel to the ice face, U_{ref} the reference
45 velocity, and ρ the water density. The drag coefficient is usually taken to be of the order $C_d \sim$
46 0.001, a value close to that of a turbulent boundary layer flow over a flat plate at high Reynolds
47 numbers (e.g. Monin et al. 1971). However, a three-dimensional wall plume can be expected
48 to exhibit strong lateral spreading similarly to what reported for the more extensively investigated
49 wall jets (Launder and Rodi 1983). This effect is attributed by these authors to the secondary flows
50 in the jet as well as to the gradients of turbulent stresses, the latter being more important (Craft
51 and Launder 2001). Assuming the turbulent stresses to be similar to those in the two-dimensional
52 boundary layer flow over a flat plate is thus not justified. A recent study (Slater et al. 2016) used
53 a larger value of $C_d = 0.01$ following Jenkins et al. (2010) who found that this larger value of C_d

54 was necessary to predict the observed melt rates of an ice shelf in Antarctica. In addition, current
 55 estimates of entrainment in wall plumes are based on experimental data and theoretical models for
 56 conical free plumes (Cowton et al. 2015; Slater et al. 2016; Mankoff et al. 2016).

57 The main focus of this study is to compare the modification of the classical plume theory for
 58 a three-dimensional turbulent wall plume against Direct Numerical Simulations (DNS) and to
 59 quantify the drag and entrainment coefficients consistent with the theory using data from DNS and
 60 existing experiments. An appropriate drag coefficient is obtained by applying the modified plume
 61 theory to our simulations and for this we use an analytical solution which, to our knowledge, is
 62 novel for 3D flows (2D analogues are reported by Gayen et al. 2016). As a first step, we consider
 63 a turbulent plume along a vertical wall without the meltwater feedback, i.e. we assume that the
 64 wall is neither a source of mass nor of buoyancy.

65 **2. Wall plume theory**

66 Following Cowton et al. (2015) we consider the wall plume as half of a conical plume and
 67 assume that it can be described by the classical system of equations suggested by Morton et al.
 68 (1956) (this approach will be justified later by means of DNS). This theory is referred hereafter as
 69 a modified MTT theory: the conservation equations for volume \tilde{Q} , momentum \tilde{M} and buoyancy \tilde{F}
 70 fluxes, are written, following Cowton et al. (2015) and Slater et al. (2016), as

$$\frac{d\tilde{Q}}{d\tilde{z}} = \frac{d}{d\tilde{z}}(\pi\tilde{b}^2\tilde{u}/2) = \pi\alpha\tilde{b}\tilde{u}, \quad (2)$$

$$\frac{d\tilde{M}}{d\tilde{z}} = \frac{d}{d\tilde{z}}(\pi\tilde{b}^2\tilde{u}^2/2) = \pi\tilde{b}^2g'/2 - 2C_d\tilde{b}\tilde{u}^2, \quad (3)$$

$$\frac{d\tilde{F}}{d\tilde{z}} = \frac{d}{d\tilde{z}}(\pi\tilde{b}^2\tilde{u}g'/2) = 0. \quad (4)$$

71 In the above, \tilde{b} is the dimensional plume radius, \tilde{u} the dimensional plume velocity (assuming
72 a top-hat velocity profile), $g' = g\Delta\tilde{\rho}/\tilde{\rho}_0$ the reduced gravity, C_d the drag coefficient and α the
73 entrainment coefficient. The latter is defined as $\tilde{u}_e = \alpha\tilde{u}$, where \tilde{u}_e is the entrainment velocity.
74 Note that, due to the presence of a wall, α is not necessarily equal to that for a conical plume.
75 Moreover, to account for a possible asymmetry in the plume shape, we introduce an ‘equivalent’
76 radius \tilde{b} (to be defined in terms of momentum and volume fluxes).

77 The system (2)-(4) is non-dimensionalized introducing the following variables $Q = \tilde{Q}/(\tilde{b}_0^2\tilde{u}_0)$,
78 $M = \tilde{M}/(\tilde{b}_0^2\tilde{u}_0^2)$, $F = \tilde{F}Fr_0^2/(\tilde{b}_0\tilde{u}_0^3)$ and $z = \tilde{z}/\tilde{b}_0$, where $Fr_0 = \tilde{u}_0/\sqrt{g'_0\tilde{b}_0}$ is the source Froude
79 number and the subscript ‘0’ indicates values at the source. Equations (2)-(3) can be rewritten as

$$\frac{dQ}{dz} = \sqrt{2\pi}\alpha M^{1/2}, \quad (5)$$

$$\frac{dM}{dz} = \frac{F_0Q}{Fr_0^2M} - \sqrt{8/\pi}C_dM^{3/2}Q^{-1}. \quad (6)$$

80 When neglecting the effect of a wall on the plume dynamics (hereafter ‘free’ plume), the drag
81 term in (6) is assumed to be zero and

$$\frac{dM}{dQ} = \frac{F_0Q}{\sqrt{2\pi}\alpha Fr_0^2M^{3/2}}, \quad (7)$$

82 which has the following analytical solution

$$M^{5/2} = M_0^{5/2} + \frac{5F_0(Q^2 - Q_0^2)}{4\sqrt{2\pi}\alpha Fr_0^2}. \quad (8)$$

83 However, in the presence of a wall the drag term in (6) should be considered, which leads to

$$\frac{dM}{dQ} = \frac{F_0Q}{\sqrt{2\pi}\alpha_w Fr_0^2M^{3/2}} - \frac{2}{\pi\alpha_w}C_d\frac{M}{Q}. \quad (9)$$

84 The solution therefore becomes (see supplementary material for derivation details)

$$M^{5/2} = \frac{5F_0Q^2}{4\sqrt{2\pi}\alpha_w Fr_0^2(1 + \frac{5C_d}{2\pi\alpha_w})} + \left(M_0^{5/2} - \frac{5F_0Q_0^2}{4\sqrt{2\pi}\alpha_w Fr_0^2(1 + \frac{5C_d}{2\pi\alpha_w})} \right) \left(\frac{Q_0}{Q} \right)^{\frac{5C_d}{\pi\alpha_w}}, \quad (10)$$

85 where α_w is the entrainment coefficient in the presence of a wall.

86 The first term on the r.h.s. of (10) grows with Q , while the second decreases; thus, for $Q \gg$
 87 Q_0 , i.e. sufficiently far from the source, the second term on the r.h.s. of (10) can be neglected.
 88 Thus, in the far field (i.e. for $M \gg M_0$ and $Q \gg Q_0$), the ratio $M^{5/2}/Q^2$ is constant for both
 89 the free (8) and wall (10) plume, and the drag and turbulent entrainment coefficients define the
 90 difference between these two cases. Since C_d is taken to be small in current models (Cowton et al.
 91 2015; Slater et al. 2016), the wall plume is assumed to behave as a half-conical free plume. This,
 92 however, should be treated with caution. We show in what follows that the drag coefficient is an
 93 order of magnitude larger than it can be expected when compared to the boundary layer flow over
 94 a flat plate.

95 The entrainment coefficient for a free plume can be obtained from the MTT theory, $b = 6/5\alpha z$,
 96 if one knows the evolution of the plume radius with the distance from the source. The far-field
 97 asymptotic solutions for the wall plume radius and velocity can be obtained substituting the first
 98 term on the r.h.s. of (10) in (5) and combining the solution with the definitions of the volume and
 99 momentum fluxes:

$$b_w = 6/5\alpha_w z, \quad (11)$$

$$u_w = \left(\frac{\alpha}{\alpha_w}\right)^{2/3} \frac{u}{\left(1 + \frac{5C_d}{2\pi\alpha_w}\right)^{1/3}}, \quad (12)$$

100 where $u = \left(\frac{5F_0}{4\pi\alpha Fr_0^2}\right)^{1/3} \left(\frac{6\alpha z}{5}\right)^{-1/3}$ is the classical MTT self-similar solution for a conical
 101 plume in a homogeneous fluid and the subscript ‘w’ indicates wall plume properties.

102 In what follow, we quantify the entrainment and drag coefficients using data from DNS. In
 103 particular, we use the radius dependence on the distance from the source to define the entrainment

104 coefficients for free and wall plumes, and then quantify the drag coefficient based on the far-field
105 solutions of (8) and (10).

106 3. Results

107 Two simulations of a turbulent vertical lazy plume in a homogeneous fluid were performed:
108 one conical plume and one wall plume. The conical plume is generated by a source volume
109 flux $2\tilde{Q}_0$ exiting from a round source of radius \tilde{b}_0 . The source Froude number of the plume is
110 $Fr_0 = \frac{\tilde{u}_0}{\sqrt{g'_0 \tilde{b}_0}} = 0.66$ and the Reynolds number $Re_0 = \frac{\tilde{u}_0 \tilde{b}_0}{\nu} = 1000$, where ν is the kinematic
111 viscosity. The Froude number chosen here corresponds to that of a lazy plume, typical of those
112 generated by a subglacial discharge. Note that a lazy plume gains velocity near the source due
113 to its buoyancy (e.g. Fischer et al. 1979), and for the Froude number used here the equivalent
114 top-hat velocity near the source becomes approximately twice as large as the source velocity, and
115 consequently, the effective Reynolds number near the source also increases nearly twice. The wall
116 plume is generated from a half-round source of radius \tilde{b}_0 attached to a wall with a total discharge
117 \tilde{Q}_0 (see visualization in Fig. 1a).

118 The DNS has been performed using the spectral element code Nek5000 (Fischer et al. 2008).
119 We consider an incompressible fluid with buoyancy modelled by the Boussinesq approximation.
120 A cylindrical domain is used to simulate the conical plume, whereas a half-cylinder is used for the
121 wall plume, with an increased resolution close to the wall. The domain radius is $10\tilde{b}_0$, while the
122 vertical length is $29\tilde{b}_0$. The resolution is less than $0.01\tilde{b}_0$ near the wall (or in terms of inner scaling
123 $\Delta x \leq 0.8x_\nu$, where $x_\nu = (Re_0 \cdot u_*)^{-1}$ is the viscous length scale, except in a small domain in the
124 vicinity of the symmetry axis where the resolution is $\Delta x \approx x_\nu$) and close to $0.01\tilde{b}_0$ in the plume,
125 thus, we resolve the viscous sublayer as well as the plume up to the Kolmogorov scale of this flow,
126 estimated as $\tilde{b}_0/Re^{3/4} \sim 0.01\tilde{b}_0$. The total number of nodes is about 29 million for the wall plume

127 and 46 million for the conical plume. We use the open (zero-gradient) boundary conditions for
128 the vertical velocity and density, combined with a sponge layer for the density fluctuations and
129 horizontal velocity at the top outflow boundary, open boundary conditions for all variables and a
130 sponge layer for the density fluctuations on the open domain sides (cf. Ezhova et al. 2017). Finally,
131 we set zero velocity and zero buoyancy flux at the wall.

132 *a. Comparison between wall plume theory and DNS results. Estimates of drag and entrainment*
133 *coefficients using the wall plume theory.*

134 The DNS results show that a wall plume indeed behaves similarly to a wall jet, being wider in
135 the direction parallel to the wall and narrower perpendicular to the wall, as illustrated by Figs. 1b,
136 c.

137 The volume and momentum fluxes are computed at horizontal cross-sections at each vertical
138 z -level as $Q = \iint U dx dy$ and $M = \iint U^2 dx dy$. The non-dimensional mean vertical velocity U is
139 an average over 50 non-dimensional time units (the eddy turnover time near the top boundary
140 is approximately 2 time units for the wall plume and 1.7 for the conical plume, where time is
141 non-dimensionalized using $t = \tilde{b}_0 / \tilde{u}_0$). The values for a half-conical free plume are obtained by
142 dividing by 2 the values from a conical plume.

143 The volume flux of the wall plume is almost identical to half of the volume flux pertaining the
144 conical plume, whereas away from the source due to the wall friction the momentum flux of the
145 wall plume is reduced by $\approx 15\%$ when compared to that of the free plume due to the wall friction
146 (Fig. 2). A similar result, i. e. same volume fluxes and significant reduction of momentum flux in
147 the presence of a wall, has been reported for three-dimensional turbulent wall jets by Namgyal and
148 Hall (2016). In agreement with the modified MTT theory solutions for wall plumes (dashed lines

149 in Fig. 2), the volume and momentum fluxes increase with distance from the source as $Q \sim z^{4/3}$
 150 and $M \sim z^{5/3}$ (see supplementary material for a detailed derivation).

151 The ‘equivalent’ plume radius is calculated at each vertical z -level as $b = \sqrt{\frac{2Q^2}{\pi M}}$ and using the
 152 relationship $b = 6/5\alpha z$ we determine the entrainment coefficient α for the two cases considered
 153 (Fig. 3). The entrainment coefficient pertaining the wall plume is slightly larger than that for the
 154 conical plume, $\alpha_w = 0.110$ and $\alpha = 0.102$, respectively. Using the entrainment coefficients, we
 155 therefore proceed with the estimate of the drag coefficient by means of (8) and (10). As discussed
 156 above, we neglect the second term on the r.h.s. of (10) and use the far-field formulations of (8) and
 157 (10) to obtain the ratio $M^{5/2}/Q^2$ for both free and wall plumes, which is given by the slope of the
 158 two curves in Fig. 3, right panel. The ratio of these two slopes, $(1 + \frac{5C_d}{2\pi\alpha_w}) \frac{\alpha_w}{\alpha} = 15.2/9.6$, gives
 159 a value of the drag coefficient $C_d \approx 0.065$, which is an order of magnitude larger than that for a
 160 boundary layer flow over a flat plate at a similar Reynolds number.

161 The most striking result of the simulations, which was not expected given the complex dynamics
 162 of the wall plume, is the similarity of the volume fluxes for a wall plume and half a conical plume
 163 (Fig. 2, left panel). In light of the latest works on jet and plume turbulence (e.g. Burrige et al.
 164 2016), one may speculate that the turbulent structures defining the entrainment in a wall plume
 165 remain similar to those in a conical plume, while only the shape of the plume ‘boundary’ changes.
 166 To support this hypothesis, the maximum velocities in the free and wall plumes are similar, and
 167 the geometric scales of the fluctuations of the plume ‘boundaries’ are similar (Fig. 4). However,
 168 the wall acts to reduce the average velocity in the wall plume as compared to the conical plume
 169 (Fig. 2) and, given the similarity of volume fluxes, the ‘equivalent’ plume radius at any given
 170 height must be larger for a wall plume (Fig. 3, left panel). Finally, given $b = 6/5\alpha z$, the latter
 171 produces an increase in entrainment coefficient for a wall plume.

172 *b. Estimates of the drag coefficient for a wall plume using the measured velocity profiles.*

173 To support the finding that the drag coefficient for a wall plume is an order of magnitude larger
174 than that for a boundary layer flow over a flat plate, we estimated the drag coefficient from
175 the mean velocity profiles at two different z cross-sections, $z = 15$ and $z = 18$.

176 We fitted the velocity profiles in the vicinity of the wall with a linear function to get the slope
177 defining the turbulent stresses (or friction velocity). The fitting function is $U = x(Re_0 \cdot u_*^2)$, cor-
178 responding to the inner scaling in the viscous sublayer. Then it is straightforward to calculate
179 the viscous scale $x_v = (Re_0 \cdot u_*^2)^{-1}$. Fig. 5 displays the velocity profiles in the inner coordinates
180 $x_+ = x/x_v$ and $U_+ = U/u_*$ at fixed y -coordinate and in the cross-sections $z = 15$ and $z = 18$. Note,
181 that u_* and x_v are different for the profiles at different fixed y -coordinates. We also show the
182 $(U_+ = x_+)$ dependence, characteristic of the viscous sublayer, and the classical log-law depen-
183 dence $(U_+ = \ln(x_+)/0.41 + 5)$.

184 As can be seen, all the velocity profiles follow the dependence typical of a viscous sublayer
185 up to $x_+ \approx 5$, in agreement with other studies on turbulent boundary layers (e.g. Monin et al.
186 1971). However, further from the wall all the velocity profiles are lower than the classical log-law
187 dependence. Note that even for the simpler case of a plane wall jet there is a discrepancy in log-
188 law constants in different studies (e.g. Banyassady and Piomelli 2015), not all studies report the
189 classical values for the parameters $\kappa = 0.41$ and $B = 5$. We are not aware of any studies comparing
190 the log-law dependence with the velocity profiles in 3D plumes or jets. However, the boundary
191 layer structure of a 3D plume is more complicated when compared to that of a 2D flow. The
192 maximum of the wall-parallel velocity in each cross-section $y = const$ moves further away from
193 the wall as the flow propagates in the z -direction, and also in each cross-section $z = const$ as the
194 plume spreads horizontally, at $|y| > 0$. Similar behaviour is reported by Namgyal and Hall (2016)

195 for a 3D wall jet. This can be considered as a smooth detachment of the flow from the wall and,
 196 in analogy with the separating (Falkner-Skan) boundary layer, might be the reason for the lower
 197 mean wall-parallel velocity in the log-law zone as compared to the classical boundary layer flow.

198 Table 1 summarizes the drag coefficients based on the maximum vertical velocity for each pro-
 199 file, $C_{dm} = (u_*/U_{\max})^2 = 0.008 - 0.024$. Further, we estimate the drag coefficients, $C_d = (u_*/u)^2$,
 200 for all the profiles based on the cross-sectional average vertical velocity, as used in the modified
 201 MTT theory. The cross-sectional average vertical velocity, defined as $u = M/Q$, yields $u_{15} = 1.45$
 202 and $u_{18} = 1.39$ in the cross-sections at $z = 15$ and $z = 18$, respectively. The drag coefficient C_d can
 203 be estimated from the friction velocity as $\int u_*^2 dy = 2C_d b u^2$. Introducing the local drag coefficient
 204 for each cross-section, $C_{d,loc}(y) = (u_*(y)/u)^2$, one can obtain $\int C_{d,loc}(y) dy = 2C_d b$. We have val-
 205 ues of $C_{d,loc}(y)$ in 7 y -cross-sections (the drag coefficient is calculated at $y = 0, 1, 2, 3$ and due to
 206 symmetry $C_{d,loc}(-y) = C_{d,loc}(y)$). Therefore, with the distance $\Delta y = 1$ between the different cross-
 207 sections, one can get an estimate for the integral: $\int C_{d,loc}(y) dy \approx \sum C_{d,i} \Delta y = (7\Delta y)(\sum C_{d,i}/7) =$
 208 $C_{d,avg} \cdot 2B$, where $2B = 7\Delta y$ and $C_{d,avg}$ is the average value of the local drag coefficient (see Table
 209 1 for $C_{d,i}$). Thus, $C_d = C_{d,avg} \cdot (B/b) \approx 0.04$ both for $z = 15$ and $z = 18$, which is lower, but still
 210 of the same order as the results obtained in the subsection 3a using the modified MTT equations.
 211 It is important to note that the value of the drag coefficient depends on the choice of the reference
 212 velocity U_{ref} , as follows from its definition, i.e. eq (1). Using the maximum and average vertical
 213 velocity as the reference velocity in the calculation above lead to differences in the drag coefficient
 214 of a factor of 3, a significant difference comparable to that obtained when changing the Reynolds
 215 number by 3-4 orders of magnitude. Hence, the choice of the drag coefficient should be consis-
 216 tent with the choice of the reference velocity when employing the MTT equations to obtain the
 217 subglacial discharge plume vertical velocity used in the melt parameterization.

218 *c. Estimates of the drag coefficient for a wall jet.*

219 In this subsection we estimate the drag coefficient using the experimental data obtained for a
 220 three-dimensional wall jet by Namgyal and Hall (2016). The drag is defined by the turbulent
 221 shear stresses, which have been observed to be similar for conical jets and plumes (van Reeuwijk
 222 et al. 2016), thus one could expect similar results for wall jets and plumes. These estimates can
 223 be used to test the sensitivity of the results to the Reynolds number, which in the experiment is
 224 $Re = 250000$, i.e. two orders of magnitude larger than in the DNS discussed in this section.

225 The solution of equation (9) for a turbulent jet is

$$M = M_0 \left(\frac{Q_0}{Q} \right)^{\frac{2C_d}{\pi\alpha_{wj}}}, \quad (13)$$

226 where α_{wj} is the wall jet entrainment coefficient. The above expression gives the momentum flux
 227 evolution with distance from the source:

$$M = M_0 \left(\sqrt{2\pi\alpha_{wj}} \left(1 + \frac{C_d}{\pi\alpha_{wj}} \right) M_0^{1/2} Q_0^{-1} z \right)^{-\frac{2C_d}{\pi\alpha_{wj}} \frac{1}{\left(1 + \frac{C_d}{\pi\alpha_{wj}} \right)}}. \quad (14)$$

228 Opposite to the wall plume results, the evolution of the wall jet ‘equivalent’ radius involves a
 229 dependence on the drag coefficient: $b_{wj} = \sqrt{\frac{2Q^2}{\pi M}} = 2\alpha_{wj} \left(1 + \frac{C_d}{\pi\alpha_{wj}} \right) z$. The ‘equivalent’ radius
 230 and momentum flux of the wall jet from the experiment of Namgyal and Hall (2016) are shown
 231 in Fig. 6. A best fit of the data in the far field allows to determine the entrainment coefficient
 232 $\alpha_{wj} \approx 0.052$, reduced when compared to the typical entrainment coefficient for a round jet found
 233 in the literature, $0.065 < \alpha_j < 0.082$ (e.g. Fischer et al. 1979), and the drag coefficient $C_d \approx 0.032$,
 234 larger than for a flat-plate boundary layer. The difference in C_d for the wall plume ($C_d = 0.065$) and
 235 jet ($C_d = 0.032$) can be related to the difference in Reynolds number between the simulations ($Re =$
 236 $1000 - 2000$) and the experiments ($Re = 250000$) and probably to near-wall buoyancy effects,
 237 absent in the case of wall jets.

238 *d. Implications of the results for the estimates of submarine glacier melt rates*

239 The drag coefficient obtained in the present study is 6.5 times larger than the value used by Slater
240 et al. (2016), $C_d = 0.01$, much higher than that used by Cowton et al. (2015), $C_d = 0.0025$, and in
241 general an order of magnitude larger than that for a boundary layer flow over a flat plate. A large
242 drag coefficient is expected given the relatively low Reynolds numbers, however the difference is
243 too large to be explained exclusively by the effect of the Reynolds number. The well-known von
244 Karman law for the boundary layer flow over a flat plate is $\frac{1}{\sqrt{c_f}} = \frac{1}{\kappa\sqrt{2}}(\ln(Re_z\sqrt{c_f}) + B_5)$, where
245 $B_5 = 1.7$, $Re_z = Uz/\nu$ and $c_f = 2C_d$ (Monin et al. 1971). If, for example, we take the cross-section
246 at $z = 15$ in the region with developed turbulence, the mean vertical plume velocity increases by
247 a factor 1.5 from its initial value, and we obtain $Re_z \approx 20000$. For this Reynolds number the drag
248 coefficient obtained from the above von Karman law for a flat plate is approximately $C_d = 0.005$,
249 an order of magnitude lower than what we obtain in the simulations. Hence, the simulations
250 results and the reasoning above suggest that also for larger Re we should expect an increased drag
251 coefficient for a wall plume. This increase in C_d is a critical factor in the current parametrization
252 for submarine melting.

253 The present study suggests that $C_d = 0.001$ is an inappropriate estimate of the drag coefficient
254 when using the modified MTT model with a top hat velocity profile. The drag decrease with
255 increasing Reynolds number can be expected to be similar to that following from the von Karman
256 law and reliably quantified for the boundary layer flow over a flat plate (e.g. Monin et al. 1971).
257 The von Karman law suggests a 4-5 times decrease of the drag coefficient from the low ($Re \sim 10^4$)
258 to high ($Re \sim 10^9$) Reynolds numbers, thus, the value of $C_d = 0.065$ obtained for $Re_z = 20000$
259 corresponds to a value $C_d = 0.01 - 0.02$ for the large Reynolds numbers, relevant to geophysical
260 flows. This is in agreement with the value 0.01 used by Slater et al. (2016). It is worth noting,

261 that the lower value of the drag coefficient due to a larger Re obtained for a wall jet in subsection
 262 3c is also consistent with that predicted by the von Karman law. In addition, given that some
 263 important phenomena, such as sediment load within the subglacial discharge plumes and glacier
 264 surface roughness, are not considered in our study, the drag coefficient relevant to geophysical
 265 flows is likely larger than 0.01-0.02.

266 We finally discuss the implications of the larger value of the drag coefficient obtained using
 267 the modified MTT theory, which is often implemented to calculate the subglacial discharge plume
 268 velocity used in the melt rate parametrizations. From the three-equation melt formulation (Holland
 269 and Jenkins 1999) the melt rate is proportional to the friction velocity, or using eq. (1) to the mean
 270 vertical plume velocity: $\dot{m} \sim u C_d^{1/2}$, where $C_d = 0.01$ is used by Slater et al. (2016) (0.0025 by
 271 Cowton et al., 2015) and u can be obtained from MTT theory neglecting the wall effects. Within
 272 the same framework, improved with eq. (12) to account for the presence of the wall, the melting
 273 rate can be written as

$$\dot{m}_w \sim u \left(\frac{\alpha}{\alpha_w} \right)^{2/3} \frac{C_d^{1/2}}{\left(1 + \frac{5C_d}{2\pi\alpha_w} \right)^{1/3}},$$

274 with the velocity u from MTT theory without a wall. This dependence of the melt rate on the
 275 drag coefficient is illustrated in Fig.7, with the melt rate normalised with that obtained with the
 276 frequently used drag coefficient $C_d = 0.0025$. Thus, the estimate of melt rate for $C_d = 0.01 - 0.02$
 277 is more than twice that obtained using $C_d = 0.0025$. Moreover, from van Kessel and Kranenburg
 278 (1996), it follows that up to a three times increase in the drag coefficient can be expected when
 279 sediments are present in the flow. Thus the melt rate can grow further to yield as much as \sim
 280 4 – 5 times that for $C_d = 0.0025$ if the sediment load and a roughness of the glacier surface are
 281 taken into account. Given the non-negligible change in melt rates, additional investigations are

282 therefore needed to characterize the dependence of C_d on Reynolds numbers and its sensitivity to
283 the sediment load.

284 **4. Conclusions**

285 We have shown that classical plume theory can form the basis of improved models of three-
286 dimensional wall plumes if the wall drag is accounted for and the entrainment coefficient is cor-
287 rected. The volume flux evolution of a wall plume is well captured already by considering half
288 of that obtained for a conical plume, which implies that the dilution of the wall plume fluid, i.e.
289 the salinity and temperature evolution with depth, should also be predicted reasonably well when
290 neglecting drag effects. The difference is only in the momentum flux which is overestimated by
291 about 10-20% if the wall drag is not accounted for. However, the coefficients parametrizing turbu-
292 lence effects for entrainment, drag and scalar transfer are important for the predictions of melting
293 rates, as these coefficients appear in the widely used three-equation melt formulation (Holland and
294 Jenkins 1999). We have shown that a consistent estimate of the drag coefficient based on the mod-
295 ified MTT theory plume velocity, and a corrected vertical velocity for wall plumes which takes
296 into account a non negligible drag coefficient (eq. 12) substantially increases the predictions for
297 melting rates near an ice wall. Furthermore, we have shown for the first time that the wall plume
298 spreads horizontally parallel to the wall and loses its axisymmetric shape (Fig. 1b, c). This impor-
299 tant aspect will produce an increase in melting when compared to that obtained with a half-conical
300 plume due to the larger area covered on an ice face by the wall plume.

301 Adding the mass and buoyancy fluxes associated with melting into the wall plume model is not
302 expected to alter our results significantly. Generally, a subglacial discharge is characterized by
303 a volume flux $Q \sim 100 \text{ m}^3 \text{ s}^{-1}$, corresponding to a ‘convection-driven melting’ regime (Jenkins
304 2011), where the contribution of submarine melting to the plume buoyancy is small. It is only

305 for a small discharge, $\approx 10 \text{ m}^3 \text{ s}^{-1}$ (Mankoff et al. 2016; Ezhova et al. 2017), that the effect of
306 submarine melting on the plume buoyancy flux cannot be neglected. Both drag and entrainment
307 are mainly influenced by the turbulent characteristics of the wall plume which, for substantial
308 subglacial discharges, should remain unchanged.

309 Our study shows that the increase in C_d for a modified MTT model of a three-dimensional wall
310 plume at large Reynolds numbers can be as high as 10 times as compared with that associated with
311 a 2D turbulent boundary layer flow ($C_d = 0.001$) and thus, can not be ignored while calculating
312 melting rates.

313 *Acknowledgments.* This work was supported by Linné FLOW Centre at KTH and by the
314 Academy of Finland Center of Excellence programme, grant no. 307331 (E.E.) and VR Swedish
315 Research Council, grant VR 2014-5001 (L.B.). Support to C.C. was given by the NSF project
316 OCE-1434041. Computer time was provided by SNIC (Swedish National Infrastructure for Com-
317 puting). Visualization and graphic analysis were performed with VisIt (Childs et al. 2012) and
318 Gnuplot.

319 **References**

320 Banyassady, R., and U. Piomelli, 2015: Interaction of inner and outer layers in plane and radial
321 wall jets. *J. Turbulence*, **16** (5), 460–483, doi:10.1080/14685248.2015.1008008.

322 Burridge, H. C., G. R. Partridge, and P. F. Linden, 2016: The fluxes and behaviour of plumes
323 inferred from measurements of coherent structures within images of the bulk flow. *Atmos.–*
324 *Ocean*, **54**, 403–417.

325 Childs, H., and Coauthors, 2012: VisIt: An End-User Tool For Visualizing and Analyzing Very
326 Large Data. *High Performance Visualization—Enabling Extreme-Scale Scientific Insight*, 357–

327 372.

328 Cowton, T., D. Slater, A. Sole, D. Goldberg, and P. Nienow, 2015: Modeling the impact of glacial
329 runoff on fjord circulation and submarine melt rate using a new subgrid-scale parameterization
330 for glacial plumes. *J. Geophys. Res. Oceans*, **120**, 796–812.

331 Craft, T. J., and B. E. Launder, 2001: On the spreading mechanism of the three-dimensional
332 turbulent wall jet. *J. Fluid Mech.*, **435**, 305–326.

333 Ezhova, E., C. Cenedese, and L. Brandt, 2017: Dynamics of a turbulent buoyant plume in a strati-
334 fied fluid: an idealized model of subglacial discharge in Greenland Fjords. *J. Phys. Oceanogr.*,
335 **47**, 2611–2630.

336 Fischer, H. B., E. List, R. Koh, J. Imberger, and N. Brooks, 1979: *Mixing in inland and coastal*
337 *waters*. Academic Press: California, USA.

338 Fischer, P. F., J. W. Lottes, and S. G. Kerkemeier, 2008: Nek5000 Web pages.
339 <http://nek5000.mcs.anl.gov>.

340 Gayen, B., R. W. Griffiths, and R. C. Kerr, 2016: Simulation of convection at a vertical ice face
341 dissolving into saline water. *J. Fluid Mech.*, **798**, 284–298, doi:10.1017/jfm.2016.315.

342 Holland, D. M., and A. Jenkins, 1999: Modelling thermodynamic ice-ocean interactions at the
343 base of an ice shelf. *J. Phys. Oceanogr.*, **29**, 1787–1800.

344 Jenkins, A., 2011: Convection-driven melting near the grounding lines of ice shelves and tidewater
345 glaciers. *J. Phys. Oceanogr.*, **41**, 2279–2294.

346 Jenkins, A., K. W. Nicholls, and H. F. Corr, 2010: Observation and parameterization of ablation at
347 the base of Ronne ice shelf, Antarctica. *J. Phys. Oceanogr.*, **40**, 2298–2312.

- 348 Launder, B. E., and W. Rodi, 1983: The turbulent wall jet - measurements and modelling. *Annu.*
349 *Rev. Fluid Mech.*, **15**, 429–459.
- 350 Mankoff, K. D., F. Straneo, C. Cenedese, S. B. Das, C. D. Richards, and H. Singh, 2016: Structure
351 and dynamics of a subglacial discharge plume in a Greenland Fjord. *J. Geophys. Res.*, **121**,
352 doi:10.1002/2016JC011764.
- 353 Monin, A. S., A. M. Yaglom, and J. L. Lumley, 1971: *Statistical Fluid Mechanics - vol 1: Me-*
354 *chanics of Turbulence*. 1st ed., The MIT Press.
- 355 Morton, B. R., G. Taylor, and J. S. Turner, 1956: Turbulent gravitational convection from main-
356 tained and instantaneous sources. *Proc. Royal Soc. London, Series A*, **234**, 1–25.
- 357 Namgyal, L., and J. W. Hall, 2016: Reynolds stress distribution and turbulence generated sec-
358 ondary flow in the turbulent three-dimensional wall jet. *J. Fluid Mech.*, **800**, 613–644.
- 359 Slater, D. A., D. N. Goldberg, P. W. Nienow, and T. R. Cowton, 2016: Scalings for submarine
360 melting at tidewater glaciers from buoyant plume theory. *J. Phys. Oceanogr.*, **46**, 1839–1855.
- 361 Straneo, F., and C. Cenedese, 2015: Dynamics of Greenlands glacial fjords and their role in cli-
362 mate. *Annu. Rev. Marine Sci.*, **7**, 89–112.
- 363 van Kessel, T., and C. Kranenburg, 1996: Gravity current of fluid mud on sloping bed. *J. Hydraul.*
364 *Eng.*, **122**, 710–717.
- 365 van Reeuwijk, M., P. Salizzoni, G. R. Hunt, and J. Craske, 2016: Turbulent transport and entrain-
366 ment in jets and plumes: A DNS study. *Phys. Rev. Fluids*, **1**, 074301.

367 **LIST OF TABLES**

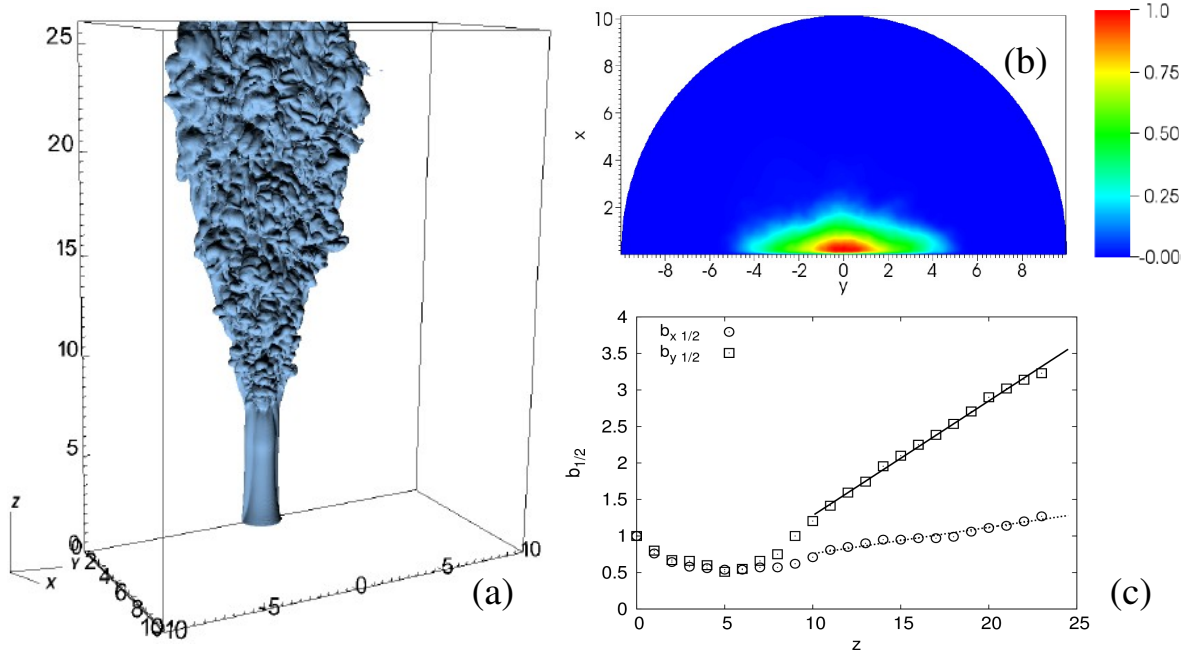
368 **Table 1.** Parameters of the logarithmic near-wall flow. 20

Parameter, $z = 15$	$y = 0$	$y = 1$	$y = 2$	$y = 3$
u_*	0.30	0.26	0.19	0.13
x_v	0.0033	0.004	0.005	0.008
U_{\max}	3.38	2.72	1.80	0.84
C_{dm}	0.008	0.009	0.011	0.024
$C_{d,i}$	0.043	0.033	0.018	0.008
Parameter, $z = 18$	$y = 0$	$y = 1$	$y = 2$	$y = 3$
u_*	0.28	0.25	0.20	0.15
x_v	0.0036	0.004	0.005	0.0065
U_{\max}	3.10	2.59	1.90	1.27
C_{dm}	0.008	0.009	0.011	0.015
$C_{d,i}$	0.041	0.033	0.021	0.012

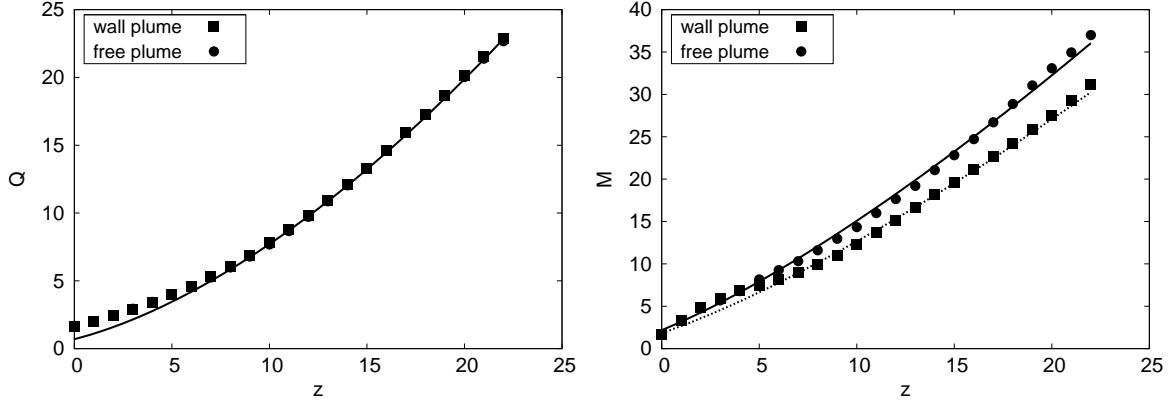
TABLE 1. Parameters of the logarithmic near-wall flow.

LIST OF FIGURES

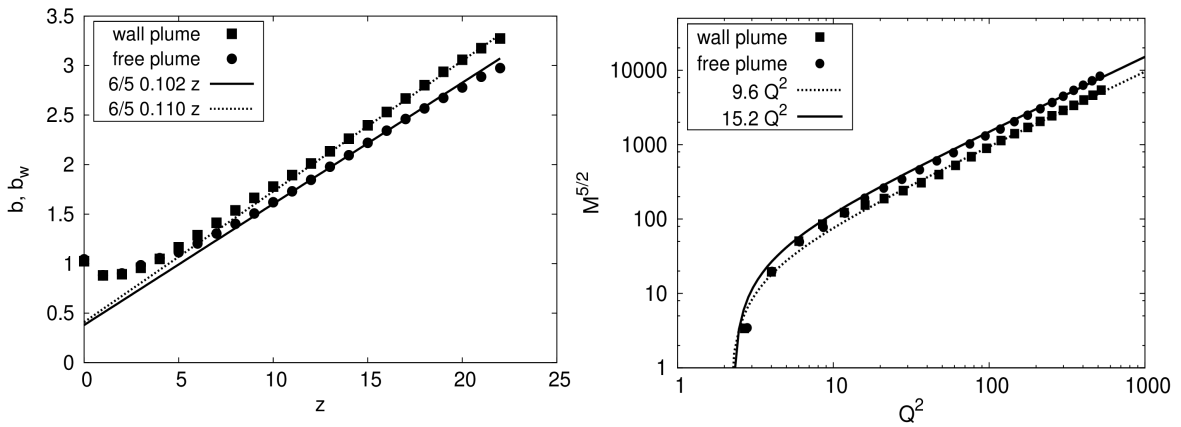
- 369
- 370 **Fig. 1.** (a) Wall plume visualized by the density contour $\rho = (\tilde{\rho} - \tilde{\rho}_{pl})/(\tilde{\rho}_{amb} - \tilde{\rho}_{pl}) = 0.99$, where
 371 $\tilde{\rho}_{pl}$ is the plume density and $\tilde{\rho}_{amb}$ is the density of the ambient fluid. (b) Mean vertical
 372 velocity at the cross-section $z = 20$ normalized with the maximum velocity in this cross-
 373 section. (c) Characteristic radii of the wall plume, $b_{1/2}$, in the x and y directions vs vertical
 374 coordinate z . $b_{1/2}$ is defined as the radius where the mean maximum velocity is halved. Best
 375 fits of the data for $z \geq 10$ have the slopes $s_x = 0.036$ and $s_y = 0.157$ 22
- 376 **Fig. 2.** Volume flux (left) and momentum flux (right) vs the vertical coordinate for the half-conical
 377 free and wall plumes. The volume flux of the wall plume is almost identical to half that
 378 of the conical plume, hence the two symbols lie on top of each other and the circles on
 379 the left panel are below the squares. Solid curves indicate the asymptotic scaling following
 380 from the classical MTT theory and valid for the conical plume; dashed curves indicate the
 381 asymptotic scaling following from the modified MTT theory and valid for the wall plume
 382 (see supplementary material). Both theories give $Q \sim z^{5/3}$ and $M \sim z^{4/3}$. The difference is
 383 in the coefficients: $Q_w/Q = \left(\frac{\alpha_w}{\alpha}\right)^{4/3} \frac{1}{\left(1 + \frac{5C_d}{2\pi\alpha_w}\right)^{1/3}} = 0.97$ (dashed and solid curves are
 384 on top of each other in the left panel); $M_w/M = \left(\frac{\alpha_w}{\alpha}\right)^{2/3} \frac{1}{\left(1 + \frac{5C_d}{2\pi\alpha_w}\right)^{2/3}} = 0.82$ with C_d ,
 385 α and α_w obtained from DNS in the present study. 23
- 386 **Fig. 3.** Left: free and wall plume radii ('equivalent' plume radius for the wall plume). Lines indicate
 387 the radius solution $b = \frac{6}{5}\alpha z$ for two different values of the entrainment coefficient. Right:
 388 $M^{5/2}$ versus Q^2 for the free and wall plumes. 24
- 389 **Fig. 4.** Statistics of the turbulent plume boundary location at $z = 15$: wall plume (upper panel) and
 390 half a conical plume (lower panel). The figures illustrate the frequency of finding the plume
 391 boundary at a certain location (in a square 0.1×0.1). Given the turbulent structure of the
 392 plume, the boundary is not always a single simple closed curve, as it encompasses turbulent
 393 eddies. The plume boundary is defined by the contour of density $\rho = (\tilde{\rho} - \tilde{\rho}_{pl})/(\tilde{\rho}_{amb} - \tilde{\rho}_{pl}) = 0.97$, where
 394 $\tilde{\rho}_{pl}$ is the plume density and $\tilde{\rho}_{amb}$ is the density of the ambient fluid. 25
- 395 **Fig. 5.** Horizontal cross-sections (left) and profiles (right) of the mean velocity parallel to the wall
 396 $U = \sqrt{\langle u \rangle^2 + \langle v \rangle^2}$ in the inner coordinates at different y locations. Upper panel:
 397 $z = 15$, lower panel: $z = 18$ 26
- 398 **Fig. 6.** Left: 'equivalent' wall jet radius vs vertical coordinate. Right: momentum flux vs vertical
 399 coordinate. Dashed and solid curves represent approximations to near-field and far-field data
 400 respectively. The data are taken from the wall jet experiment by Namgyal and Hall (2016). 27
- 401 **Fig. 7.** Melt rate dependence on the drag coefficient. The melt rate is normalized with that obtained
 402 using $C_d = 0.0025$ 28



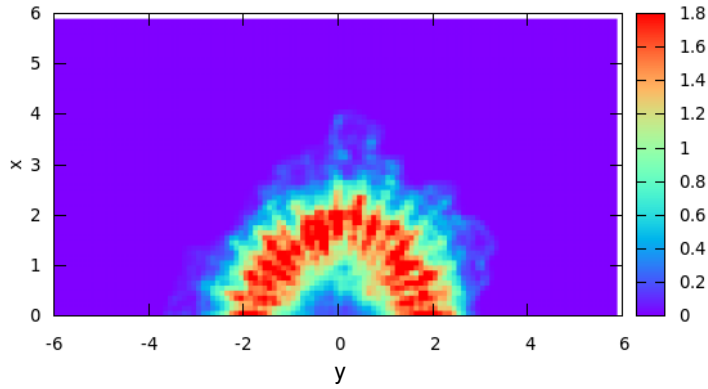
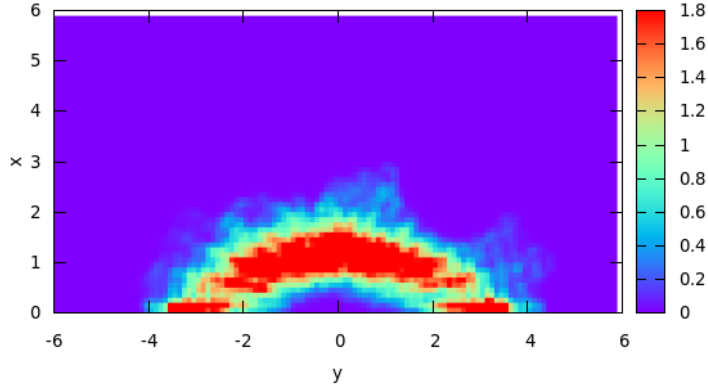
403 FIG. 1. (a) Wall plume visualized by the density contour $\rho = (\tilde{\rho} - \tilde{\rho}_{pl}) / (\tilde{\rho}_{amb} - \tilde{\rho}_{pl}) = 0.99$, where $\tilde{\rho}_{pl}$ is the
 404 plume density and $\tilde{\rho}_{amb}$ is the density of the ambient fluid. (b) Mean vertical velocity at the cross-section $z = 20$
 405 normalized with the maximum velocity in this cross-section. (c) Characteristic radii of the wall plume, $b_{1/2}$, in
 406 the x and y directions vs vertical coordinate z . $b_{1/2}$ is defined as the radius where the mean maximum velocity is
 407 halved. Best fits of the data for $z \geq 10$ have the slopes $s_x = 0.036$ and $s_y = 0.157$.



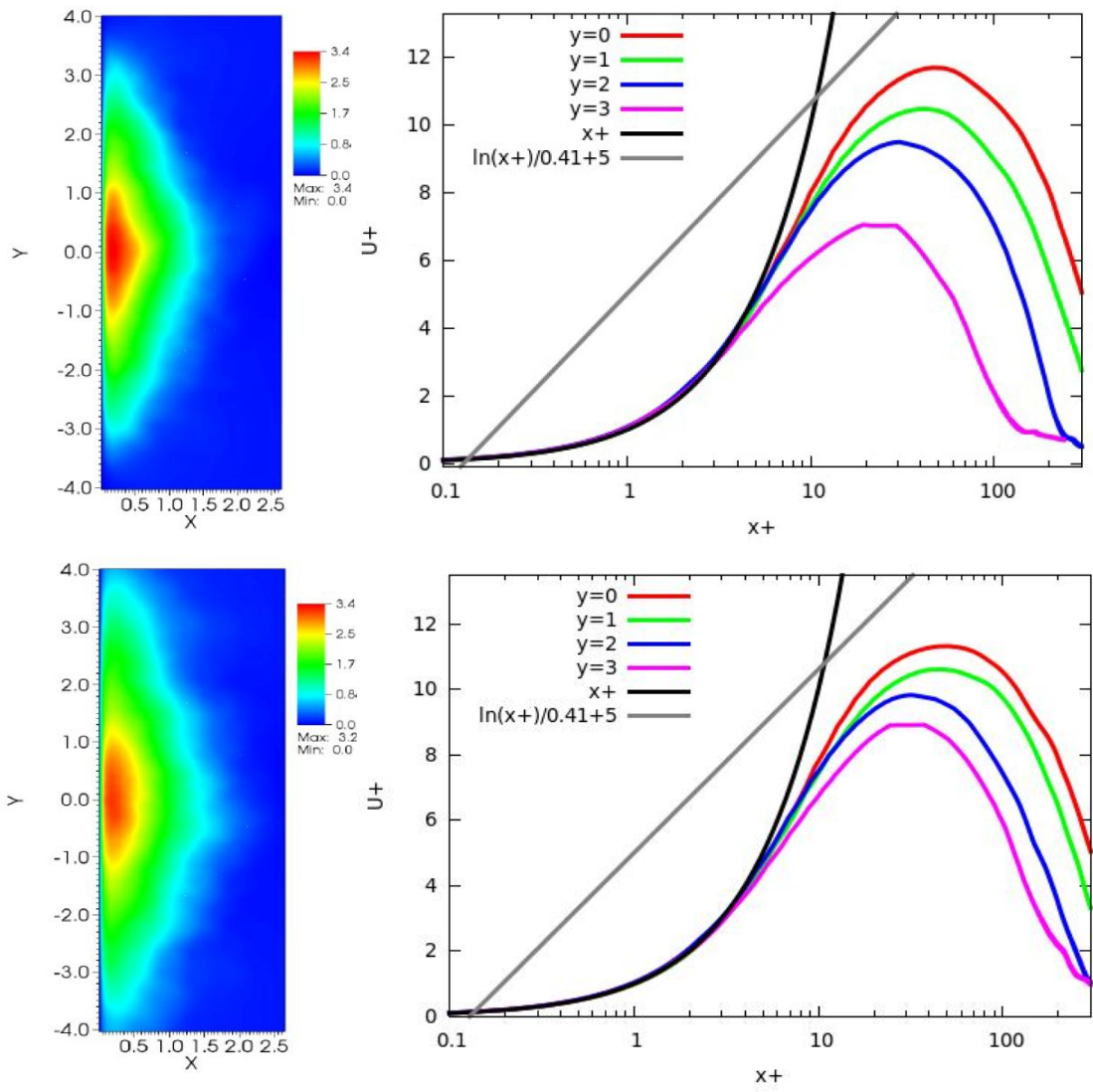
408 FIG. 2. Volume flux (left) and momentum flux (right) vs the vertical coordinate for the half-conical free and
 409 wall plumes. The volume flux of the wall plume is almost identical to half that of the conical plume, hence
 410 the two symbols lie on top of each other and the circles on the left panel are below the squares. Solid curves
 411 indicate the asymptotic scaling following from the classical MTT theory and valid for the conical plume; dashed
 412 curves indicate the asymptotic scaling following from the modified MTT theory and valid for the wall plume
 (see supplementary material). Both theories give $Q \sim z^{5/3}$ and $M \sim z^{4/3}$. The difference is in the coefficients:
 413 $Q_w/Q = \left(\frac{\alpha_w}{\alpha}\right)^{4/3} \frac{1}{\left(1 + \frac{5C_d}{2\pi\alpha_w}\right)^{1/3}} = 0.97$ (dashed and solid curves are on top of each other in the left panel);
 414
 415 $M_w/M = \left(\frac{\alpha_w}{\alpha}\right)^{2/3} \frac{1}{\left(1 + \frac{5C_d}{2\pi\alpha_w}\right)^{2/3}} = 0.82$ with C_d , α and α_w obtained from DNS in the present study.



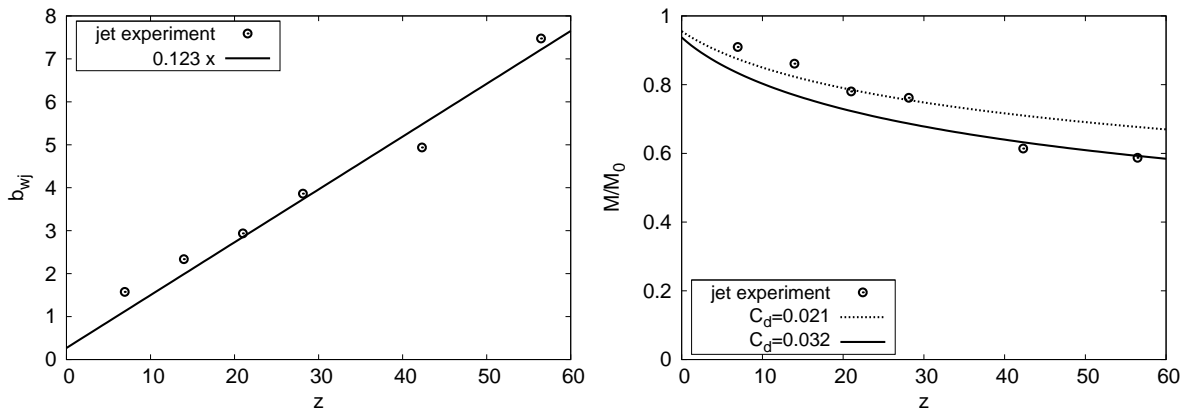
416 FIG. 3. Left: free and wall plume radii ('equivalent' plume radius for the wall plume). Lines indicate the
 417 radius solution $b = \frac{6}{5} \alpha z$ for two different values of the entrainment coefficient. Right: $M^{5/2}$ versus Q^2 for the
 418 free and wall plumes.



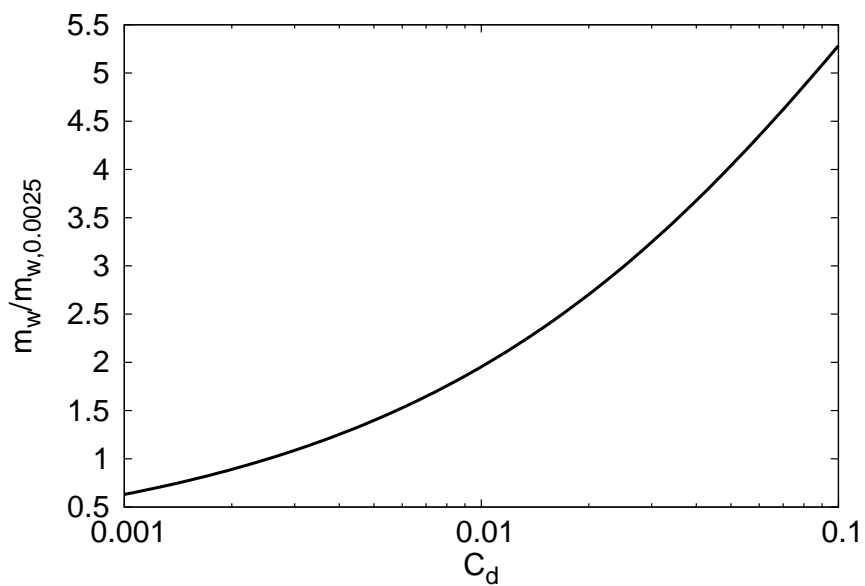
419 FIG. 4. Statistics of the turbulent plume boundary location at $z = 15$: wall plume (upper panel) and a
 420 conical plume (lower panel). The figures illustrate the frequency of finding the plume boundary at a certain
 421 location (in a square 0.1×0.1). Given the turbulent structure of the plume, the boundary is not always a single
 422 simple closed curve, as it encompasses turbulent eddies. The plume boundary is defined by the contour of density
 423 $\rho = (\tilde{\rho} - \tilde{\rho}_{pl}) / (\tilde{\rho}_{amb} - \tilde{\rho}_{pl}) = 0.97$, where $\tilde{\rho}_{pl}$ is the plume density and $\tilde{\rho}_{amb}$ is the density of the ambient fluid.



424 FIG. 5. Horizontal cross-sections (left) and profiles (right) of the mean velocity parallel to the wall $U =$
 425 $\sqrt{\langle u \rangle^2 + \langle v \rangle^2}$ in the inner coordinates at different y locations. Upper panel: $z = 15$, lower panel: $z = 18$.



426 FIG. 6. Left: 'equivalent' wall jet radius vs vertical coordinate. Right: momentum flux vs vertical coordinate.
 427 Dashed and solid curves represent approximations to near-field and far-field data respectively. The data are taken
 428 from the wall jet experiment by Namgyal and Hall (2016).



429 FIG. 7. Melt rate dependence on the drag coefficient. The melt rate is normalized with that obtained using
430 $C_d = 0.0025$.